33RD CONGRESS
OF THE INTERNATIONAL COUNCIL
OF THE AERONAUTICAL SCIENCES
STOCKHOLM, SWEDEN, 4-9 SEPTEMBER, 2022

ICAS 2022 SWEDEN

ANALYSIS OF A LAMINAR SEPARATION BUBBLE ON A NACA0009 AIRFOIL AT DIFFERENT BACKGROUND DISTURBANCE LEVELS

J. Simon Kern, Ardeshir Hanifi & Dan S. Henningson

FLOW, Department of Engineering Mechanics, KTH Royal Institute of Technology, Stockholm, Sweden

Abstract

The laminar separation bubble (LSB) forming on a symmetric NACA0009 airfoil at a steady pitch angle of 8° and Reynolds number $\mathrm{Re} = 2.0 \cdot 10^5$ under the influence of free-stream disturbances is computed using high-fidelity large-eddy simulations. Two disturbance levels are considered corresponding to cruise conditions achievable in low free-stream turbulence wind tunnels and higher disturbance levels typical of larger, conventional wind tunnels. The extracted flow fields are Fourier transformed in the spanwise direction and then each spanwise mode is analysed using Spectral Proper Orthogonal Decomposition to extract the dominant structures in the flow exhibiting spatio-temporal coherence. Since LSBs are known to be sensitive to external disturbances as well as self-excited absolute instabilities, the analysis of the effect of free-stream disturbances on the separation bubble is crucial for understanding the bubble dynamics and to relate results from simulations to experiments in applications where certain levels of inflow disturbance are unavoidable.

Keywords: Unsteady aerodynamics, laminar separation bubble, LES, SPOD

1. Introduction

Laminar separation bubbles (LSBs) are a common phenomenon on lifting surfaces operating at comparatively low Reynolds numbers, from airfoils on micro air vehicles to compressor blades in gas turbines. The LSBs are usually induced by an adverse pressure gradient in the boundary layer and are highly unstable. The dynamics of the resulting flow structures has been analysed extensively for several decades both theoretically and experimentally. Several studies have documented that LSBs strongly amplify external disturbances ([1, 2]) but also exhibit self-excited instabilities [3]. In view of this sensitivity of LSBs and their importance for aerodynamic performance and in particular their role in the onset of dynamic stall ([4]) it is important to analyse the effect of different levels of background disturbances on the dynamics of LSBs in numerical studies.

In this work, we consider a NACA0009 airfoil at a chord-based Reynolds number of $\mathrm{Re} = 2.0 \cdot 10^5$ and a steady pitch angle of 8° for which an LSB with turbulent reattachment exists close to the leading edge. Two highly-resolved LES simulations are performed with two different background disturbance levels influencing the LSB. The resulting structures are analysed using the Spectral Proper Orthogonal Decomposition (SPOD).

2. Numerical methods and mesh generation

The numerical simulations are performed using the open-source code Nek5000 ([5]) using a high-order spectral element method to solve the incompressible Navier-Stokes equations directly with an implicit relaxation-term filtering for stabilisation. Within each spectral element, the solution is expanded in terms of Lagrange polynomials at the Gauss-Lagrange-Lobatto (GLL) points in each coordinate direction. The equations are solved using a Galerkin approximation scheme in the $\mathrm{P}_N - \mathrm{P}_{N-2}$ formulation. The non-linear terms are treated explicitly via third-order extrapolation scheme and the viscous terms are treated implicitly using a third-order backward-differencing scheme. All

quantities are non-dimensionalised with the inflow velocity U and the chord length c yielding the flow time scale $t = c/U$. The computational strategy in this work, both in terms of numerical methods and meshing, are similar to the approach used in [6].

2.1 Mesh generation

The computational setup was designed to obtain well-resolved data of the laminar separation bubble at a steady angle of attack of 8° and also allow for a subsequent active pitching of the airfoil in a fashion similar to [7]. This is done in order to be able to analyse the effect of the background noise level both in the steady case (present work) and subsequently also in the more challenging pitching case using the same setup. In order to minimise the influence of the boundary conditions on the solution for both static and dynamics cases while incurring a reasonable computational cost, an intermediate computational domain size was chosen to reconcile the requirements ($3.5c$ in radial direction, $0.1c$ along the span (following [7]).

A structured conformal C-type computational mesh is constructed around the airfoil containing $1.8 \cdot 10^5$ spectral elements in 3D. With a polynomial order of $N = 7$ for the velocity ($N = 5$ for the pressure) in each coordinate direction, the simulation has roughly 1 billion degrees of freedom.

During the mesh generation process, in order to estimate the maximum turbulent wall shear-stress τ_w on the airfoil, 2D RANS simulations using the Menter k-Ω SST turbulence model ([8]) were carried out under the same conditions using ANSYS Fluent® v18.2. These estimates were the basis for the spectral-element mesh where the following design criteria were applied for the near wall region. The superscript $+$ indicates viscous scaling.

- Suction side, $0 < x/c < 0.2$ (LSB): $x^+ < 15$, $y^+ < 0.5$. Note that resolution was defined based on the maximum τ_w as a worst case scenario even for the laminar sections.
- Suction side, $0.2 < x/c < 1$: $x^+ < 20$, $y^+ < 1$. The streamwise resolution is progressively relaxed over the airfoil to reduce the cell count but refined close to the trailing edge.
- Pressure side: The flow is expected to be laminar and the streamwise resolution downstream of the stagnation point is relaxed to $x^+ < 25$ on average.

The initial two-dimensional mesh is generated in ANSYS ICEM CFD™ v18.2 and subsequently coarsened in radial direction away from the airfoil surface. The conformal coarsened mesh structure close to the leading edge is shown in Fig. 1 (top). In spanwise direction, the mesh was extruded to yield a nominal resolution at the wall of $z^+ = 9$. In order to reduce the cell count, the 12th spectral element layer (at approx. $0.075c$ from the airfoil surface) in the extruded mesh was conformally coarsened in spanwise direction (halving the spanwise resolution further away from the wing, see Fig. 1, bottom). The wall-normal distance was chosen such that the entire LSB is contained in the resolved part of the mesh. The de facto resolution was checked a posteriori using the wall shear-stress statistics gathered during the simulations.

2.2 Free-stream disturbance level

As the domain boundaries are very far from the leading edge, the usual method of imposing free-stream turbulence directly on the velocity boundary condition at the inflow (see e.g. [6]) would incur unmanageable computational cost due to the high resolution needed to resolve the scales as the turbulence develops and the added simulation time for it to cross the domain. An alternative method avoiding this constraint by introducing realistic free-stream turbulence using a body force (see, e.g., [9]) is also not applicable since it requires the laminar baseflow to be known a priori whereas in this work, the full solution is time-dependent. In view of these difficulties and considering that the disturbance amplitudes are very low, it was chosen, instead of forcing a specific spectrum, to force with bandwidth limited white noise upstream of the leading edge and let the flow adapt. The disturbances are introduced using a volume forcing in a box roughly $0.1c$ upstream of the airfoil to give the fluctuations time to adapt to the flow and whose amplitude is tuned to obtain the desired disturbance levels

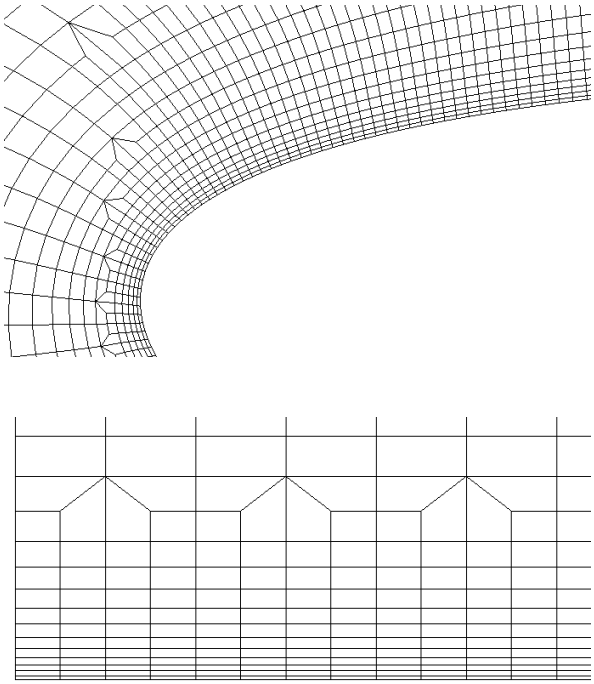

Figure 1 – **Top**: Numerical grid in the $xy-$plane close to the leading edge. **Bottom**: Spanwise resolution and coarsening close to the wing. Only the spectral elements are shown.

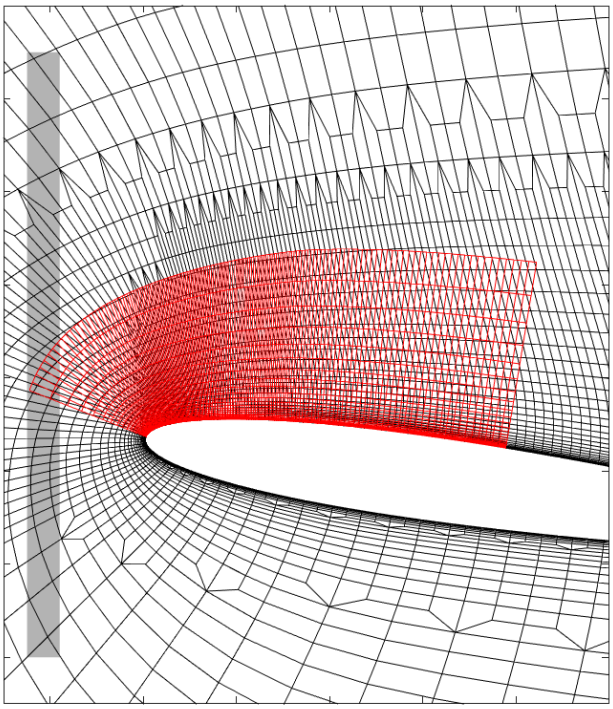

Figure 2 – Close-up of the mesh around the airfoil (black), the forcing region (grey) and the interpolation mesh for SPOD (red, only every 4th gridline is shown).

at the leading edge of the airfoil. The region where the forcing is applied is shown as a shaded area in Fig. 2.

Two background noise levels were chosen for the comparison. The value of the turbulence intensity is computed from the time and span averaged statistics at the point $x_0 = (0, 0.05)$ (see also Fig. 3) close to the leading edge as

$$\mathrm{Tu} = \frac{\sqrt{\frac{1}{3}(\overline{u^2} + \overline{w^2} + \overline{w^2})}}{U}, \tag{1}$$

where the lowercase letters refers to fluctuating quantities and the overbar denotes averaging in time and along the span. Note that the disturbance generation used here is not expected to yield realistic FST spectra. The two considered cases differ only in the value of the disturbance levels, measured at the point x_0 and are defined as:

Case I: A low background noise level with $\mathrm{Tu} = 0.02\%$ at the leading edge which corresponds to the disturbance levels observed in low free-stream turbulence academic wind tunnels or on actual aircraft in cruise conditions.

Case II: A slightly higher background noise level with $\mathrm{Tu} = 0.05\%$ at the leading edge which is achievable in conventional wind tunnels that are routinely used in the development stages of aeronautical applications.

It was chosen not to run a case with no background disturbance because the disturbances stemming from the mesh are difficult to quantify and are likely to influence the laminar separation bubble that is known to be extremely sensitive to noise. Furthermore, a completely noise-free environment is never encountered in practical applications. Instead of trying to mimic a specific energy spectrum for the disturbances that might vary considerably from one configuration to the next, a more generic white noise forcing was chosen due to its simplicity and reproducibility.

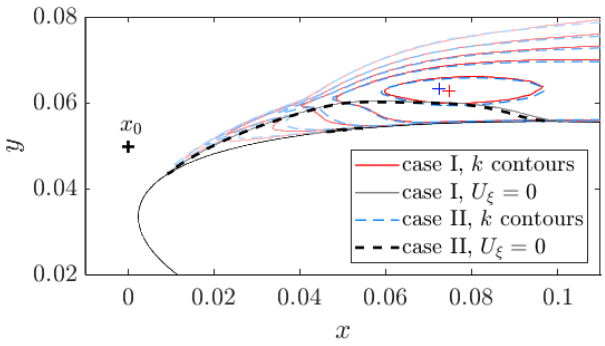

Figure 3 – Distribution of the turbulence kinetic energy k in case I (red) and case II (blue) with levels $k = [2, 6, 20, 60, 200] \cdot 10^{-3}$. The full grey and dashed black lines indicate the edges of the recirculation zones and the coloured crosses the point of maximum k in each case.

3. Flow statistics of the laminar separation bubbles subjected to free-stream disturbances

Once the initial transients have passed, the 2D flow statistics are averaged over a simulation time of $T = 1.63$ as well as across the span. The data aggregation is performed using the statistics toolbox in Nek5000 described in [10], adapted to deal with non-uniform meshes in the homogeneous direction. Some details on the alterations are given in appendix A. From the averaged velocity data we compute the turbulence kinetic energy k as

$$k = \frac{1}{2}\left(\overline{u^2} + \overline{v^2} + \overline{w^2}\right) \tag{2}$$

Comparing the spatial extent of the laminar separation bubble in each case based on the edge of the recirculation bubble as well as the distribution of turbulence kinetic energy k, we observe that in case II with the higher disturbance level, the bubble is slightly flatter and shorter overall. At the same time, the boundary layer transition that begins at about $x/c = 0.04$, evidenced by the kink in the k contours, happens faster due to the increased background disturbance level. The maximum of turbulence kinetic energy in case II, reaching 5% higher values than in case 1 ($k_{\max,I} = 0.274$), moves upstream by $0.3\%c$ (or roughly 3% of the bubble length), the same distance that the mean reattachment point moves. The mean dividing streamline and the location of the maxima are shown in Fig. 3. Interestingly, the levels of turbulence kinetic energy convected into the nominally laminar part of the recirculation bubble are reduced in case II although the maximum average backflow is increased by 4% to 41.6% of U at the point marked by the blue cross in Fig. 4. These backflow velocities are far in excess of $15-20\%$ which are the values found in literature for the onset of absolute instability based on local analysis ([11, 12]) and are even higher than the instantaneous backflow peaks encountered during the pitching of a natural laminar flow (NLF) airfoil by Negi et al. ([6]) that transiently exhibits local absolute instability. The present LSB is therefore likely also absolutely unstable. Note that the backflow is computed in body fitted (ξ, η)-coordinates to account for the surface curvature.

The space-time diagrams of the two cases (Fig. 5) show that the turbulent part of the LSBs are highly unsteady and highlights a second small separation bubble at around $x/c = 0.05$ generated by a weak secondary vortex that is hardly visible in Fig. 4 due to its small thickness. Furthermore, this highly unsteady vortex shrinks and extends less towards the leading edge as the disturbance level increases which is likely the cause for the reduced advection of turbulence kinetic energy into the laminar part of the separation bubble. The pressure coefficient is very similar in both bases, albeit case II is on average shifted to lower pressures (0.8% increase of maximum suction) due to an increase of the flow speed over the bubble (see inset Fig. 5), and one can clearly discern the paths of the Kelvin-Helmholtz (KH) rolls that are continuously shed from the separated shear layer at around $x/c = 0.05$ and moving downstream. The different KH rolls vary in strength and the passage of rolls with lower local pressure is a major driver of the unsteadiness of the turbulent reattachment location.

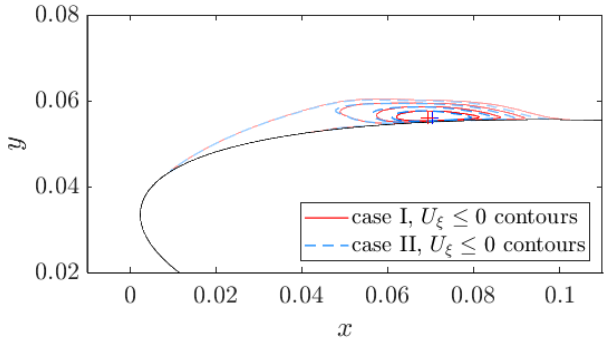

Figure 4 – Backflow distribution in case I (red) and case II (blue) with levels $U_\xi = [0, -0.1, -0.2, -0.3]$. The zero contours correspond to the full grey and dashed black lines in Fig. 3. The coloured crosses indicate the point of maximum backflow in each case.

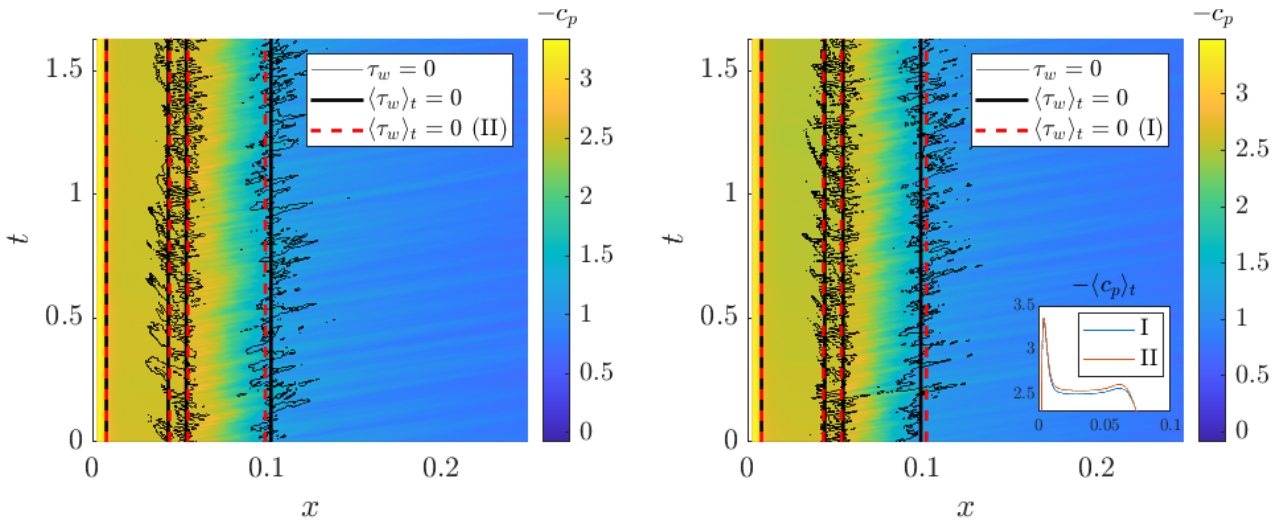

Figure 5 – Space-time diagrams of the pressure coefficient near the LSB for case I (left) and case II (right). The black lines are the contours of vanishing instantaneous wall shear-stress. The vertical lines mean separation/reattachment points, the dashed line corresponding to the comparison case. The inset on the right shows the mean pressure coefficient.

Furthermore, the peak variance of both pressure and wall shear-stress signals during the boundary layer transition is on average 60% larger in the case with high background disturbance (not shown). This peak is reached at around $x/c = 0.08$ in both cases.

The unsteadiness of the instantaneous flow field also becomes obvious when considering the flow visualizations for each case (see Fig. 6). The KH rolls are clearly visible as well as their nearly instantaneous loss of two-dimensionality that initiates the rapid breakdown into small-scale turbulence across the LSB. Although the flow dynamics are very similar close to the separation and transition, the λ_2-structures show a low frequency fluctuation of the developing turbulent boundary layer that is superimposed on the turbulent structures and seems to vary from one case to the other. In order to quantify these differences objectively, we perform spectral proper orthogonal decomposition of the three-dimensional flow fields.

4. Spectral Proper Orthogonal Decomposition

Spectral Proper Orthogonal Decomposition (SPOD) is an empirical, data-driven analysis tool to extract structures from flow data that are coherent in both space and time. The framework extends the ideas of classical or space-only Proper Orthogonal Decomposition (POD) for statistically stationary

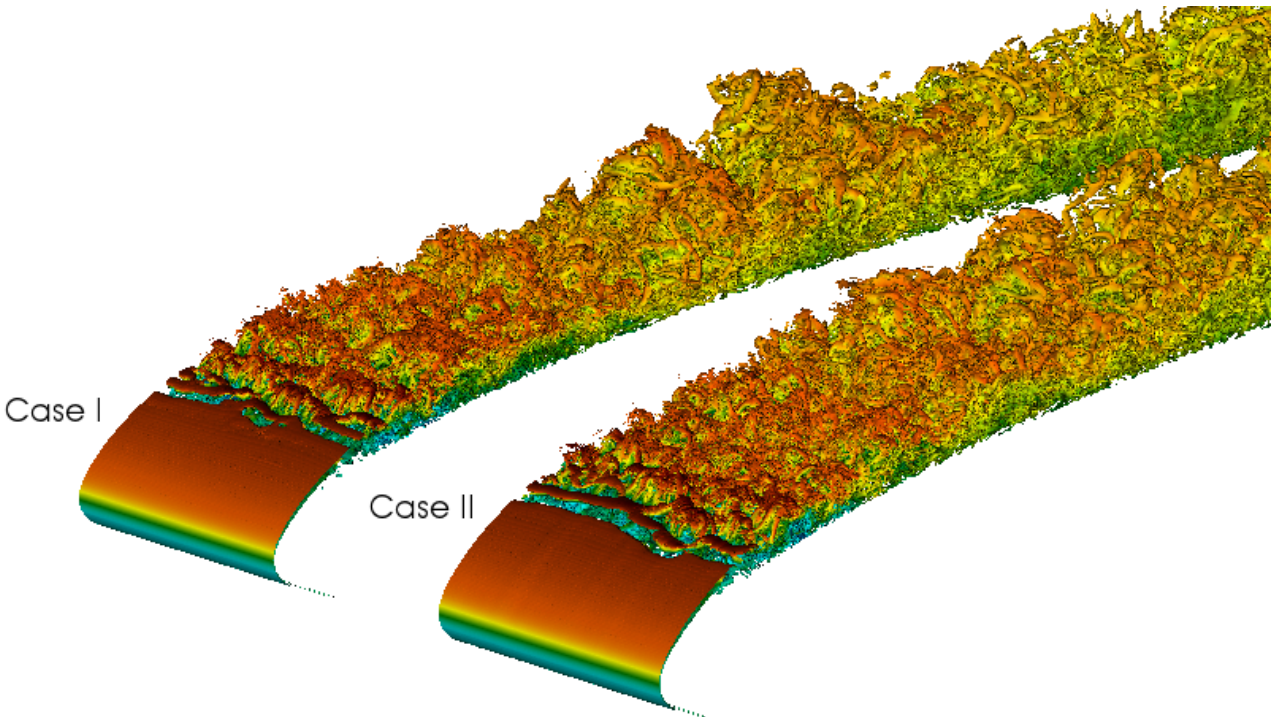

Figure 6 – Snapshots of the λ_2-structures colored by axial velocity. The flow is from left to right.

flows to generate a set of orthogonal modes at each frequency that optimally capture the energy (variance) present in the data ([13]). Since the flow case is also homogeneous in spanwise direction, the 3D data from the simulation are first Fourier-transformed in z and the decomposition subsequently applied to the Fourier coefficients for each spanwise frequency.

In this work the raw data for the SPOD computation was extracted at intervals of $\Delta t = 8.0 \cdot 10^{-4}$ during the main run of the simulation (after the initial transients have passed) that covers the full simulation span of $T = 1.63$ time units yielding a total of 2048 3D snapshots of the flow for each case. In order to reduce the amount of data the flow fields are interpolated onto a smaller mesh covering the domain of interest (red mesh in right of Fig. 1). The interpolating mesh has roughly the same spatial resolution than the main simulation in all directions and has equidistant spacing along the span. After the Fourier transform in the homogeneous direction, only the leading 7 modes (including the mean flow at frequency 0) are retained since the high-order modes do not exhibit spatial coherence.

The algorithm used in this work is based on the Matlab code from [14] adapted to the current setup. The SPOD modes are computed using the method of snapshots, dividing the 2048 flow fields for each spanwise frequency into 31 bins of length $T_0 = T/16$ with 50% overlap containing 128 snapshots each for the temporal Fourier transform. The lowest frequency that we can resolve is therefore $f_0 = 1/T_0 \approx 9.8$ which roughly corresponds to the low-frequency boundary layer modulation we can observe in Fig.6 which have a group velocity close to U. The mean is not included in the SPOD calculation.

The resulting full SPOD energy spectra for $k_z = 0$ are shown in the left panel of Fig.7. We can clearly see the peak at $f = 68.4$ (marked with a diamond in the center panel) that corresponds to the KH shedding frequency that is sharper and more pronounced in case II. Consequently, the leading SPOD mode for the KH-rolls accounts for 35 and 48% of the total variance (sum of the eigenvalues at this frequency) in cases I and II, respectively (see the right panel). The corresponding SPOD modes are shown in Fig. 8c and 8g and are virtually indistinguishable. This indicates that the increased disturbance level leads to faster growth of the same structures (rolls) and thus a more pronounced frequency selection. The Strouhal number of the KH rolls, based on the mean recirculation bubble thickness ($D = 0.0066c$) and the inflow velocity, is $\mathrm{St} = fD/U = 0.45$. Considering the different span-

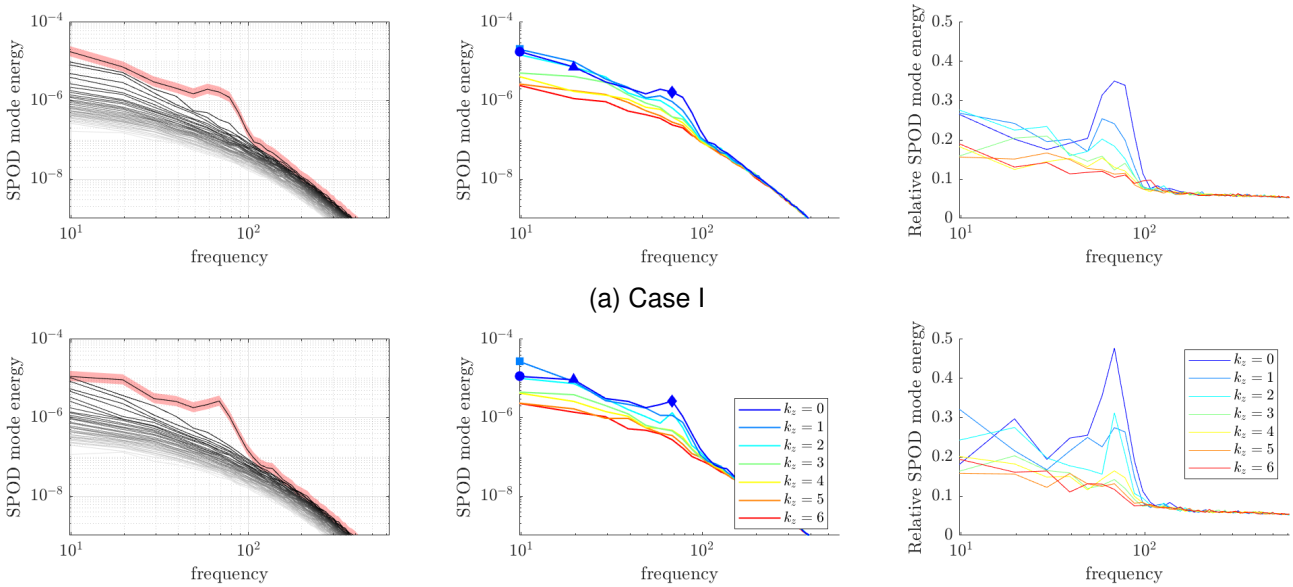

(a) Case I

(b) Case II

Figure 7 – SPOD spectra for cases I and II (rows 1 and 2, respectively). **Left:** Full spectrum for $k_z = 0$ (red area is the 95% confidence interval shown only for the leading mode). **Center:** Leading SPOD eigenvalue for different spanwise wavenumbers. For the points marked with symbols the fields are shown in Fig. 8. **Right:** Proportion of energy concentrated in leading mode for each frequency and wavenumber.

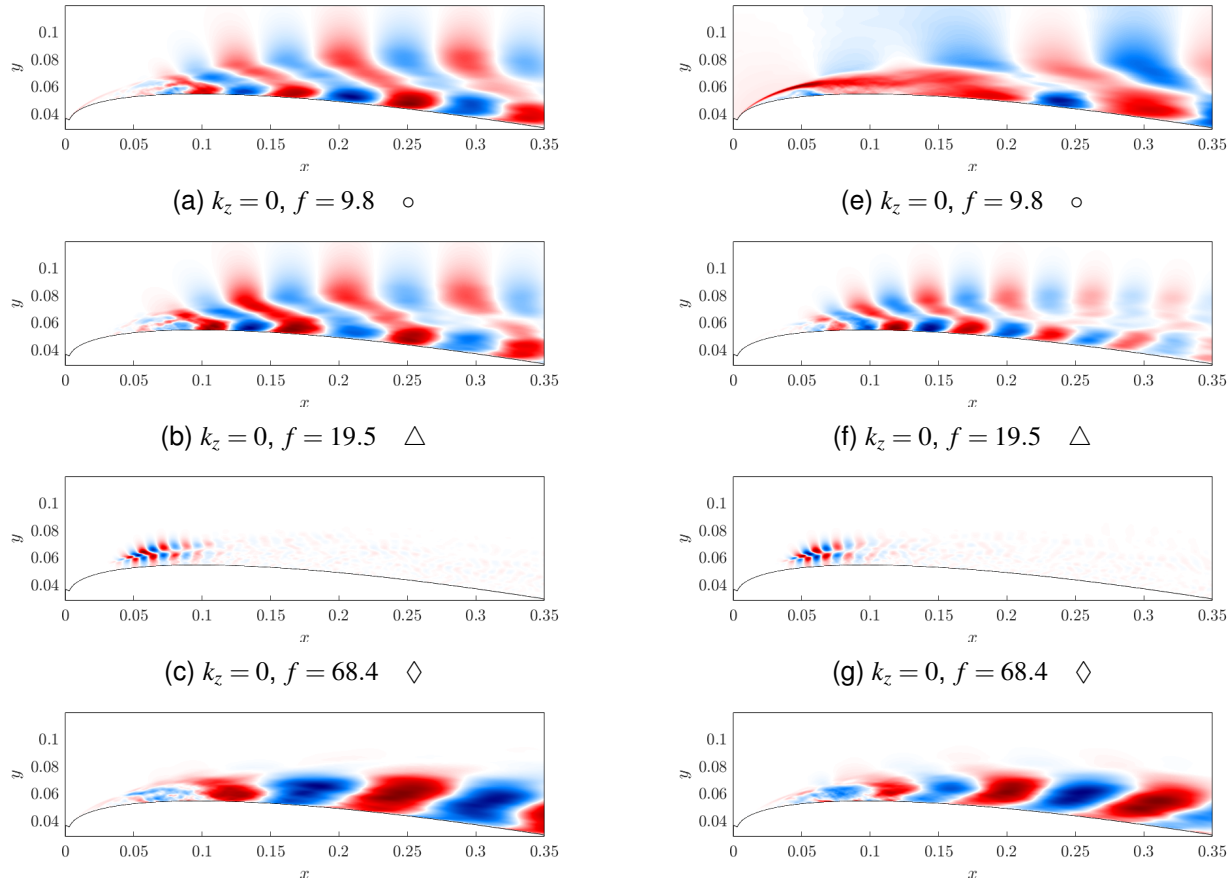

(a) $k_z = 0,\ f = 9.8$ ○

(b) $k_z = 0,\ f = 19.5$ △

(c) $k_z = 0,\ f = 68.4$ ◇

(d) $k_z = 2,\ f = 9.8$ □

(e) $k_z = 0,\ f = 9.8$ ○

(f) $k_z = 0,\ f = 19.5$ △

(g) $k_z = 0,\ f = 68.4$ ◇

(h) $k_z = 2,\ f = 9.8$ □

Figure 8 – x-velocity component of the leading SPOD mode for different spanwise wavenumbers and frequencies. The symbol relates to the location in Fig. 7. **Left:** Case I. **Right:** Case II.

wise wavenumbers (center panel) we observe that the peak corresponding to the KH-rolls disappears for $k_z > 2$ as the initially 2D rollers quickly lose coherence as they disintegrate into turbulence. The limit of coherence at $k_z = 2$ can also be seen in the λ_2-structures in the shear layer in Fig.6. For higher spanwise wavenumbers, like also for frequencies beyond $f \approx 100$, there is no dominant coherent structure in the turbulent flow which translates into a SPOD spectrum with eigenvalues of similar magnitude.

The bulk of the energy is contained in the low-frequency modes with the spectrum for case II noticeably flattening off for low frequencies (with the exception of $k_z = 1$). But, in this region, the leading mode is less dominant overall. Fig. 8 shows the spatial structure of the leading SPOD mode at a few selected frequencies. We see that in case I the dominant structures for a range of low frequencies are similar. When the disturbance level increases (case II) this structure only persists for $k_z = 1$ and a low-frequency "breathing" of the LSB becomes important (Fig. 8e). In general, the perturbation structures at low frequencies are waves that initially lean against the mean shear and grow downstream by extracting energy from the mean flow in a process similar to the Orr-mechanism which can be clearly seen in Fig. 8d and 8h. Similar observations have been made in e.g. turbulent jets ([15]).

5. Conclusion

The flow around a NACA0009 airfoil at at angle of attack of 8° is simulated using high-fidelity LES for two different low background disturbance levels that are both common in real flight conditions and wind tunnel experiments. The particular interest of this study is the small laminar separation bubble that forms at the leading edge and is highly sensitive to external disturbances. While the variation of the averaged quantities is small, the instantaneous dynamics of the LSB change considerably. When the disturbance amplitude is increased The Kelvin-Helmholtz rolls formed on the separated shear layer become stronger and a low-frequency breathing of the LSB occurs. This analysis shows that for certain configurations like the laminar separation bubbles, the flow is so sensitive to even minute extermal disturbances that the dynamics change even for apparently negligible variations of the background disturbance level. One direct consequence of these results is that care must be taken when attempting to compare simulation results to experiments if the former do not consider free-stream disturbances.

6. Funding

Financial support for this work was provided by the European Research Council (ERC) under grant agreement 694452-TRANSEP-ERC-2015-AdG and by VINNOVA in the project LaFloDes under grant agreement 2019-05369. The simulations were performed on resources of the Swedish National Infrastructure of Computing (SNIC) at Linköping University (LiU).

7. Contact Author Email Address

skern@kth.se

8. Copyright Statement

References

[1] L. E. Jones, R. D. Sandberg, and N. D. Sandham, “Stability and receptivity characteristics of a laminar separation bubble on an aerofoil,” *J. Fluid Mech.*, vol. 648, pp. 257–296, 2010.

[2] O. Marxen and D. S. Henningson, “The effect of small-amplitude convective disturbances on the size and bursting of a laminar separation bubble,” *J. Fluid Mech.*, vol. 671, pp. 1–33, 2011.

[3] D. Rodríguez, E. M. Gennaro, and L. F. Souza, “Self-excited primary and secondary instability of laminar separation bubbles,” *J. Fluid Mech.*, 2020.

[4] A. Sharma and M. Visbal, "Numerical investigation of the effect of airfoil thickness on onset of dynamic stall," *J. Fluid Mech.*, vol. 870, pp. 870–900, 2019.

[5] P. F. Fischer, J. W. Lottes, and S. G. Kerkemeier, "Nek5000 web page," 2008.

[6] P. Negi, R. Vinuesa, A. Hanifi, P. Schlatter, and D. S. Henningson, "Unsteady aerodynamic effects in small-amplitude pitch oscillations of anairfoil," *International Journal of Heat and Fluid Flow*, vol. 71, p. 378, 2018.

[7] S. I. Benton and M. R. Visbal, "The onset of dynamic stall at a high, transitional reynolds number," *J. Fluid Mech.*, vol. 861, pp. 860–885, 2019.

[8] R. B. Langtry and F. R. Menter, "Correlation-based transition modeling for unstructured parallelized computational fluid dynamics codes," *AIAA journal*, vol. 47, no. 12, pp. 2894–2906, 2009.

[9] K. Durovic, P. Schlatter, A. Hanifi, and D. S. Henningson, "Generation of three-dimensional homogeneous isotropic turbulence," tech. rep., Department of Engineering Mechanics, KTH Royal Institute of Technology, 2022.

[10] R. Vinuesa, A. Peplinski, M. Atzori, L. Fick, O. Marin, E. Merzari, P. Negi, A. Tanarro, and P. Schlatter, "Turbulence statistics in a spectral-element code: a toolbox for high-fidelity simulations," Tech. Rep. TRITA-SCI-RAP 2018:010, Department of Engineering Mechanics, KTH Royal Institute of Technology, 2018.

[11] D. A. Hammond and L. G. Redekopp, "Local and global instability properties of separation bubbles," *European journal of mechanics, B, Fluids*, vol. 17, no. 2, pp. 145–164, 1998.

[12] M. Alam and N. D. Sandham, "Direct numerical simulation of 'short' laminar separation bubbles with turbulent reattachment," *J. Fluid Mech.*, vol. 410, pp. 1–28, 2000.

[13] A. Nekkanti and O. T. Schmidt, "Frequency-time analysis, low-rank reconstruction and denoising of turbulent flows using spod," *J. Fluid Mech.*, vol. 926, 2021.

[14] O. T. Schmidt and T. Colonius, "Guide to spectral proper orthogonal decomposition," *AIAA journal*, vol. 58, no. 3, pp. 1023–1033, 2020.

[15] E. Pickering, G. Rigas, P. A. S. Nogueira, A. V. G. Cavalieri, O. T. Schmidt, and T. Colonius, "Lift-up, Kelvin–Helmholtz and Orr mechanisms in turbulent jets," *J. Fluid Mech.*, vol. 896, p. A2, 2020.

A Spatial averaging of statistics data on non-uniform grids

The statistics toolbox for Nek5000 ([10]) gathers the time and span averaged statistics at runtime performing the spatial averaging continuously within the local spectral elements to reduce the storage allocation and minimise communication. When the data is written to disk, the statistics are averaged across the span using global communicators. This approach is efficient but requires the spanwise average to be computed at runtime and the elements to be uniform in the homogeneous direction. In order to accommodate the mesh used in this work, the elements that are non-uniform in the spanwise direction are identified and marked during initialisation and mapped onto so-called ghost elements occupying the same volume that are uniform in span. During the averaging process, the data is interpolated onto the ghost elements (using a spectrally accurate interpolation scheme) which are then averaged in the standard fashion. The structure, including the distribution of the GLL points in the spectral elements, of the simulation and interpolation meshes (ghost elements) is shown in Fig. 9. Note here that the GLL points inside the ghost elements and the rest of the mesh are aligned in the homogeneous direction. This interpolation is performed locally and only involves less than 5% of the elements and thus only has a negligible computational overhead.

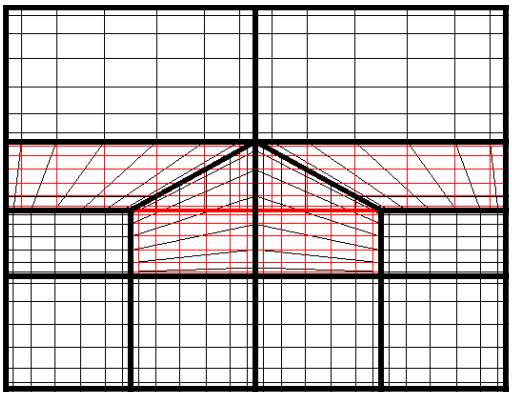

Figure 9 – Illustration of a yz-slice of the conformal simulation mesh (black, spectral elements and GLL points are shown in thick and thin black lines, respectively) and the non-conformal but z-uniform ghost elements (red) that replace the distorted elements for spanwise (horizontal) averaging.